Received: 4 September 2023 | Revised: 5 June 2024 | Accepted: 12 October 2024

DOI: 10.1002/gamm.202370008

ORIGINAL ARTICLE

A continuum chemo-mechano-biological model for in-stent restenosis with consideration of hemodynamic effects

Kiran Manjunatha[1] | **Anna Ranno**[2] | **Jianye Shi**[1] | **Nicole Schaaps**[3] | **Pakhwan Nilcham**[3] | **Anne Cornelissen**[3] | **Felix Vogt**[3] | **Marek Behr**[2] | **Stefanie Reese**[1]

[1]Institute of Applied Mechanics, RWTH Aachen University, Aachen, Germany

[2]Chair for Computational Analysis of Technical Systems, RWTH Aachen University, Aachen, Germany

[3]Department of Cardiology, Vascular Medicine and Intensive Care, RWTH Aachen University, Aachen, Germany

Correspondence
Kiran Manjunatha, Institute of Applied Mechanics, RWTH Aachen University, Mies-van-der-Rohe-Str. 1, 52074 Aachen, Germany.
Email: kiran.manjunatha@ifam.rwth-aachen.de

Anna Ranno, Chair for Computational Analysis of Technical Systems, RWTH Aachen University, Schinkelstraße 2, 52062 Aachen, Germany.
Email: ranno@cats.rwth-aachen.de

Funding information
Deutsche Forschungsgemeinschaft, Grant/Award Numbers: 333849990, 395712048, 403471716, 465213526

Abstract

The occurrence of in-stent restenosis following percutaneous coronary intervention highlights the need for the creation of computational tools that can extract pathophysiological insights and optimize interventional procedures on a patient-specific basis. In light of this, a modeling framework encompassing the chemo-mechano-biological interactions in the arterial wall and the effects of hemodynamic perturbations is introduced in this work.

KEYWORDS

growth factors, growth modeling, hemodynamics, multiphysics, neointimal hyperplasia, oscillatory shear index, relative residence time, wall shear stress

1 | INTRODUCTION

A heightened prevalence of cardiovascular diseases in the current population can be attributed to an unhealthy lifestyle. Smoking, consumption of processed foods, and lack of physical activity are among the factors that constitute such a lifestyle. In this context, one of the prominent cardiovascular diseases with a high mortality rate is atherosclerotic cardiovascular disease (ASCVD). ASCVD is characterized by the accumulation of substantial plaque within the coronary arteries leading to restricted blood flow. This potentially results in ischemic episodes and, in severe instances, myocardial infarction.

To address the symptoms of ASCVD and restore blood flow in blocked coronary arteries, the percutaneous coronary intervention (PCI) procedure involving the insertion of stents is utilized. But PCI is associated with two inherent risks: (1) stent thrombosis (ST), and (2) in-stent restenosis (ISR). The current study is focussed on ISR.

1.1 | Pathophysiology of ISR

Friction between the PCI balloon or stent and the arterial wall, coupled with the arterial stretching that occurs during PCI, causes a partial or complete removal of the endothelial monolayer. This endothelial layer serves as a protective barrier, preventing the exposure of underlying contents to the bloodstream. However, the denudation of this layer results in the exposure of extracellular materials to the blood flow, initiating a series of inflammatory reactions. These responses include platelet aggregation, the release of cytokines and substances that promote cell division into the subendothelial area, prompting the migration and multiplication of smooth muscle cells (SMCs), and the infiltration of circulating monocytes.

Consequently, unregulated tissue growth is triggered, resulting in obstructions to the blood flow. This outcome directly contradicts the purpose of PCI. The process is referred to as neointimal hyperplasia.

Additionally, the perturbations in the hemodynamics within the coronary artery, brought about by stent-implantation, lead to low/oscillatory wall shear stress (WSS) on the vessel lining. This then leads to a dysfunctional behavior of the endothelial cells (ECs) and consequently enhances the development of neointima [7, 21, 24, 31].

Despite the substantial reduction in the occurrence of ISR achieved through the use of modern drug-eluting stents (DESs), the problem persists due to the individualized nature of patients' inflammatory responses and the limitations of the medical system in fine-tuning PCI procedures to match these responses appropriately.

1.2 | State of the art computational models

Numerous computational frameworks have been proposed to simulate ISR. These models can be broadly categorized as follows:

(a) Approaches that combine cellular automata (CA) with agent-based modeling (ABM) [10, 40–42];
(b) Phenomenological continuum mechanical models [11, 12, 17];
(c) Multiscale multiphysics-based chemo-mechano-biological continuum models [5, 9].

However, computational models that incorporate the impact of drug pharmacokinetics and pharmacodynamics, particularly in the context of drugs integrated within drug-eluting stents (DESs), have been relatively limited in the literature. A handful of works, [6], [36], and [30] to name a few, have delved into these aspects.

Another area of current research is the choice of a constitutive model for blood, which is relevant in the context of a fully coupled fluid-structure interaction (FSI) model for ISR. In large arteries with physiological flow, blood can be approximated as a homogeneous Newtonian fluid without altering the overall flow characteristics. For capillary arteries or in pathological conditions, shear thinning effects and blood damage cannot be neglected [1, 2, 14–16, 26, 39]. One of the most relevant blood flow indicators to assess the well-being of the artery wall is WSS, and hence an FSI framework that incorporates the effects of WSS on the pathophysiology of ISR is of utmost interest.

The current study therefore contributes to the advancement of computational methodologies for modeling ISR. It specifically focuses on the intricate interplay between crucial mediators and the kinetics of drug elution, providing a substantial resolution that can yield valuable insights and facilitate the customization of interventional procedures. Additionally, to aid the development of an FSI framework, hemodynamics aspects of stent implantation and the methodology for extraction of key blood flow indicators are established.

1.3 | Overview

The authors herein present two constituents that make up a fully resolved FSI framework for modeling ISR. This includes the development of a multiphysics model for the arterial wall that captures the interactions between significant mediators of ISR in combination with a hemodynamic computation setup that derives key blood flow quantities that influence the restenotic process.

2 | MODEL DESCRIPTION

2.1 | Arterial wall model

2.1.1 | Continuum mechanical modeling

The arterial wall is assumed to be composed of two layers, the media and the adventitia, each consisting of two helices of collagen fibers embedded in an isotropic ground matrix. To model the volumetric growth involved in the restenotic process, we adopt the well-known multiplicative split of the deformation gradient $\boldsymbol{F}$ [34], that is,

$$\boldsymbol{F} = \boldsymbol{F}_e\, \boldsymbol{F}_g, \tag{1}$$

where $\boldsymbol{F}_g$ maps the referential geometry to an intermediate stress-free grown state, while $\boldsymbol{F}_e$ achieves the compatibility of deformations. Upon further decomposition of the growth part $\boldsymbol{F}_g$ into a pure stretch part and a pure rotational part [18], that is,

$$\boldsymbol{F}_g = \boldsymbol{R}_g\, \boldsymbol{U}_g, \tag{2}$$

we can rewrite the decomposition in Equation (1) as

$$\boldsymbol{F} = \underbrace{\boldsymbol{F}_e\, \boldsymbol{R}_g}_{:=\boldsymbol{F}_*}\, \boldsymbol{U}_g = \boldsymbol{F}_*\, \boldsymbol{U}_g. \tag{3}$$

The right Cauchy–Green tensor associated with the mapping $\boldsymbol{F}_*$ shall then be

$$\boldsymbol{C}_* = \boldsymbol{F}_*^T\, \boldsymbol{F}_* = \boldsymbol{U}_g^{-1}\, \boldsymbol{C}\, \boldsymbol{U}_g^{-1}. \tag{4}$$

The Helmholtz free energy per unit volume in the reference configuration is additively split into an isotropic part associated with the isotropic ground matrix, and an anisotropic part corresponding to the collagen fibers, that is,

$$\psi = \psi_{\text{iso}} + \psi_{\text{ani}}. \tag{5}$$

With $\boldsymbol{U}_g$ as an internal variable, the Helmholtz free energy for the isotropic ground matrix, encompassing the behaviors of the smooth muscle cells, elastins, and proteoglycans, is prescribed to be of the Neo-Hookean form as

$$\psi_{\text{iso}}(\boldsymbol{C}, \boldsymbol{U}_g) = \frac{\mu}{2}(\text{tr}\ \boldsymbol{C}_* - 3) - \mu\ \ln\ J_* + \frac{\Lambda}{4}\left(J_*^2 - 1 - 2\ \ln\ J_*\right), \tag{6}$$

where $J_* = \sqrt{\det(\boldsymbol{C}_*)}$. We herein embed the directionality of the helices of collagen fibers via the generalized structural tensor approach [13], defining them to be of the form

$$\boldsymbol{H}_i = \kappa\ \boldsymbol{I} + (1 - 3\ \kappa)\ \boldsymbol{a}_{0i} \otimes \boldsymbol{a}_{0i} \tag{7}$$

for each helix ($i = 1, 2$). Here κ refers to the dispersion parameter, and $\boldsymbol{a}_{0i}$ to the collagen orientations in the reference configuration. The Helmholtz free energy associated with the collagen fibers is then chosen to be of the form

$$\psi_{\text{ani}}(\boldsymbol{C}, \boldsymbol{H}_1, \boldsymbol{H}_2, c_c^0) = \frac{k_1}{2k_2} \sum_{i=1,2} \left(\exp\left[k_2 \langle E_i \rangle^2\right] - 1\right), \tag{8}$$

where

$$E_i := \boldsymbol{H}_i : \boldsymbol{C} - 1, \tag{9}$$

and the stress-like parameter k_1 is scaled according to the local collagen concentration in the reference configuration (c_C^0), that is,

$$k_1 = \bar{k}_1 \left(\frac{c_C^0}{c_{C,eq}} \right), \tag{10}$$

where $\bar{k}_1$ is the stress-like material parameter for healthy collagen and $c_{C,eq}$ is the homeostatic collagen concentration in a healthy artery.

Volumetric growth is achieved via the direct prescription of the growth stretch tensor $\boldsymbol{U}_g$ [27] based on the amount of dispersion κ, which can be histologically inferred. Two forms are proposed herein, namely,

$$\begin{aligned} (\kappa \approx 0): \quad & \boldsymbol{U}_g := \boldsymbol{I} + (\vartheta - 1)\, \boldsymbol{\gamma} \otimes \boldsymbol{\gamma}, \quad \boldsymbol{\gamma} := \frac{\boldsymbol{a}_{01} \times \boldsymbol{a}_{02}}{\|\boldsymbol{a}_{01} \times \boldsymbol{a}_{02}\|}, \quad \vartheta := \frac{\rho_S^0}{\rho_{S,eq}} \\ (\kappa > 0): \quad & \boldsymbol{U}_g := \vartheta\, \boldsymbol{I}, \quad \vartheta := \left(\frac{\rho_S^0}{\rho_{S,eq}} \right)^{1/3}, \end{aligned} \tag{11}$$

where ρ_S^0 is the local SMC density in the reference configuration, and $\rho_{S,eq}^0$ is the SMC density in a healthy homeostatic vessel.

2.1.2 | Balance equations for mediators

The balance equations for the concentrations of PDGF (c_P), TGF-β (c_T), ECM with collagen as the primary constituent (c_C), and the drug (c_D), in addition to the densities of SMCs (ρ_S) and ECs (ρ_E) are set up to model the chemo-biological interactions involved in neointimal hyperplasia. The specific details can be found in [28] while short descriptions are provided in the section that follows. The advection-reaction-diffusion equation forms the basis for the aforementioned balance of mediators, the general form of which in the Eulerian description is

$$\underbrace{\left.\frac{\partial \phi}{\partial t}\right|_{\boldsymbol{x}}}_{\text{rate}} + \underbrace{\operatorname{div}(\phi\, \boldsymbol{v})}_{\text{advection}} = \underbrace{\operatorname{div}(k\, \operatorname{grad}\phi)}_{\text{diffusion}} + \underbrace{\overset{\text{source}}{\mathcal{R}} - \overset{\text{sink}}{\mathcal{S}}}_{\text{reaction}}. \tag{12}$$

The particularized balance equations for the mediators are set up based on the physiological response of a stented artery in an inflammatory setting and are summarized to be as follows.

PDGF: It is a constituent of the platelets that aggregate on the sites of endothelial denudation. They are additionally secreted by monocytes that invade the denuded area and interact in their differentiated state as macrophages with the stent surface as well as cellular constituents. SMC itself secretes PDGF in the presence of TGF-β. The parameter r_η modulates what amount of PDGF secretion is attributed to TGF-β modulated secretion by SMCs and secretion by infiltrating monocytes. Rapamycin drastically reduces the monocyte infiltration which is accounted for by the function f_{P1}. PDGF is depleted once the associated ligand-receptor complexes are formed on the SMCs and internalized. TGF-β, at high concentrations restricts the aforementioned complex formation which is taken care of by the scaling function f_{P2}. The balance equation hence is

$$\left.\frac{\partial c_P}{\partial t}\right|_{\boldsymbol{x}} + \operatorname{div}\left(c_P\, \boldsymbol{v}\right) = \underbrace{\operatorname{div}\left(D_P\, \operatorname{grad}\, c_P\right)}_{\text{diffusion}} + \underbrace{\left((1 - r_\eta) + r_\eta\, f_{P1}(c_D)\right)\eta_P \rho_S\, c_T}_{\substack{\text{secretion by SMCs} \\ \text{and macrophages}}} - \underbrace{\varepsilon_P\, f_{P2}(c_T)\, \rho_S\, c_P}_{\substack{\text{receptor} \\ \text{internalization}}}, \tag{13}$$

where

$$f_{P1}(c_D) := \exp(-l_{P1}\, c_D) \in [0, 1], \tag{14}$$

$$f_{P2}(c_T) := \frac{1}{1 + \exp\left(l_{P2}\left(c_T - c_{T,th}\right)\right)} \quad \in [0, 1]. \tag{15}$$

TGF-β: It is considered merely diffusive in the artery wall while being depleted by the formation of the ligand-receptor complexes on the SMCs. This leads to the balance equation

$$\left.\frac{\partial c_T}{\partial t}\right|_{\boldsymbol{x}} + \operatorname{div}\left(c_T\ \boldsymbol{v}\right) = \underbrace{\operatorname{div}\left(D_T\ \operatorname{grad}\ c_T\right)}_{\text{diffusion}} - \underbrace{\varepsilon_T\ \rho_S\ c_T}_{\substack{\text{receptor}\\ \text{internalization}}}. \tag{16}$$

ECM: Collagen, the key constituent of the ECM is secreted by SMCs which sense a degraded ECM environment. The more the degradation, the higher the rate of secretion. Matrix metalloproteinases (MMPs) which are upregulated in the presence of PDGF result in the cleavage of collagen and degradation of the ECM environment. The governing equation hence is

$$\left.\frac{\partial c_C}{\partial t}\right|_{\boldsymbol{x}} + \operatorname{div}\left(c_C\ \boldsymbol{v}\right) = \underbrace{\eta_C \rho_S \left(1 - \frac{c_C}{c_{C,th}}\right)}_{\substack{\text{secretion by}\\ \text{synthetic SMCs}}} - \underbrace{\varepsilon_C\ c_P\ c_C}_{\substack{\text{MMP-induced}\\ \text{degradation}}}. \tag{17}$$

Drug: Rapamycin and its analogs are the prevalent compounds embedded in modern DESs. They attach to specific receptors on the SMCs to induce their antiproliferative and anti-inflammatory effects. Their diffusion and depletion are intended to be modeled via the equation

$$\left.\frac{\partial c_D}{\partial t}\right|_{\boldsymbol{x}} + \operatorname{div}\left(c_D\ \boldsymbol{v}\right) = \underbrace{\operatorname{div}\left(D_D\ \operatorname{grad}\ c_D\right)}_{\text{diffusion}} - \underbrace{\varepsilon_{D1}\ \rho_S\ c_D}_{\substack{\text{receptor}\\ \text{internalization}}}. \tag{18}$$

SMC: The SMCs are considered to be the drivers of the volumetric growth and hence are modeled with high fidelity taking into account their transport and proliferation processes. SMCs move up the gradient in cytokines, PDGF in this case, in a degraded ECM scenario. This is modeled by the *chemotaxis* term. Also, unless there is a fully healed ECM to anchor the SMCs, they tend to move down the gradient in collagen concentration. This is modeled by the *haptotaxis* term. This movement is in fact triggered by an upregulated PDGF presence. Hence a function f_{S1} is introduced that activates the haptotactic movement beyond a certain level of PDGF.

$$\begin{aligned}\left.\frac{\partial \rho_S}{\partial t}\right|_{\boldsymbol{x}} + \operatorname{div}\left(\rho_S\ \boldsymbol{v}\right) = &\underbrace{-\operatorname{div}\left(\rho_S\ \overbrace{\chi_{S1}\left(1 - \frac{c_C}{c_{C,th}}\right)\operatorname{grad} c_P}^{\boldsymbol{v}_{S1}}\right)}_{\text{chemotaxis}} + \underbrace{\operatorname{div}\left(\rho_S\ \overbrace{\chi_{S2}\, f_{S1}(c_P)\operatorname{grad} c_C}^{-\boldsymbol{v}_{S2}}\right)}_{\text{haptotaxis}}\\ &+ \underbrace{\eta_S\, f_{S2}(c_P)\, f_{S3}(c_T)\, f_{S4}(c_D)\, \rho_S \left(1 - \frac{c_C}{c_{C,th}}\right)}_{\text{proliferation}},\end{aligned} \tag{19}$$

where

$$f_{S1}(c_P) := \frac{1}{1 + \exp\left(-l_{S1}\left(c_P - c_{P,th}\right)\right)} \quad \in [0,1]. \tag{20}$$

SMC proliferation is dependent on a multitude of factors which necessitates the introduction of several functions into the associated source term, namely

$$f_{S2}(c_P) := 1 - \exp(-l_{S2}\ c_P) \in [0,1], \tag{21}$$

$$f_{S3}(c_T) := \frac{1}{1 + \exp\left(l_{S3}\left(c_T - c_{T,th}\right)\right)} \quad \in [0,1], \tag{22}$$

$$f_{S4}(c_D) := 1 - \frac{1}{100}\left(\frac{A_S\, c_D^{\alpha}}{c_D^{\alpha} + B_S^{\alpha}}\right) \quad \in [0,1]. \tag{23}$$

Here, function f_{S2} saturates the proliferativity of SMCs beyond a certain concentration of PDGF. f_{S3} acts as a TGF-β dependent switch for SMC proliferation. Finally f_{S4} takes into account the Hill-type dependence of the reduction in proliferation of SMCs due to their interaction with rapamycin.

EC: The endothelium is modeled as a monolayer on the luminal side of the arterial wall. The balance equation for the ECs is hence only active on the luminal surface and is set to be of the form

$$\left.\frac{\partial \rho_E}{\partial t}\right|_{\boldsymbol{x}} + \mathrm{div}_\Gamma\left(\rho_E\, \boldsymbol{v}_\Gamma\right) = \underbrace{\mathrm{div}_\Gamma\left(D_E\, \mathrm{grad}_\Gamma\, \rho_E\right)}_{\text{diffusion}} + \underbrace{\eta_E\, f_{E1}(c_D)\, \rho_E \left(1 - \frac{\rho_E}{\rho_{E,eq}}\right)}_{\text{proliferation}} - \underbrace{\varepsilon_E\, f_{E2}(c_D)\, \rho_E}_{\text{apoptosis}}, \tag{24}$$

where

$$f_{E1}(c_D) := 1 - \frac{1}{100}\left(\frac{A_E\, c_D^{\beta}}{c_D^{\beta} + B_E^{\beta}}\right) \quad \in [0,1], \tag{25}$$

$$f_{E2}(c_D) := 1 - \exp(-l_E\, c_D) \in [0,1]. \tag{26}$$

The proliferation term is constructed to be of the logistic fashion, that is, the closer the EC population to the healthy value, the lower the rate of proliferation. The function f_{E1} takes into account the inhibition of EC proliferation due to the presence of rapamycin. Also, rapamycin is known to exaggerate the apoptosis of ECs and hence a drug-dependent apoptosis function f_{E2} is introduced in the sink term.

We herein employ the Lagrangian equivalent of the general form in Equation (12), which is obtained from the transformation of the terms involved, given by

$$J^{-1}\, \dot{\phi^0} = J^{-1}\mathrm{Div}\left[k\, \boldsymbol{C}^{-1}\left(\mathrm{Grad}(\phi^0) - \left(\frac{\phi^0}{J}\right)\mathrm{Grad}\, J\right)\right] + \mathcal{R}_0 - \mathcal{S}_0. \tag{27}$$

The quasi-static balance of linear momentum

$$\mathrm{Div}\,(\boldsymbol{F}\,\boldsymbol{S}) + \boldsymbol{B} = \boldsymbol{0}, \tag{28}$$

forms the basis for modeling the structural response of the arterial wall, $\boldsymbol{S}$ being the second Piola–Kirchhoff stress tensor, and $\boldsymbol{B}$ the body force vector in the reference configuration. The inertial effects of the added mass that results in the slow growth process are hence ignored.

2.1.3 | Coupling the chemo-biological interactions to the continuum mechanical setup

The solutions to Equations (17) and (19) in the Lagrangian coordinates will furnish the collagen concentration and the SMC density in the reference configuration. These can then be utilized to vary the compliance of the vessel wall per Equation (10) and prescribe the evolution of the growth stretch tensor as given in Equation (11).

2.2 | Blood flow model

Blood flow is modeled by means of incompressible Navier-Stokes equations and a Newtonian constitutive model. At this validation stage, walls are assumed to be rigid. *No-slip* boundary conditions are imposed on the artery wall Γ_w and on the stent inner surface Γ_{stent}. On Γ_{out}, we impose for the velocity to be perfectly orthogonal to the outflow surface.

The boundaries are depicted in Figure 1A. The inflow velocity imposed on Γ_{in} is given by the function $\mathbf{g}$ as:

$$\mathbf{g}(\mathbf{x},t) = C(A(t))Q(t)\left(1 - \frac{|\mathbf{x}|^2}{r_0^2}\right)\mathbf{n} \quad \text{on } \Gamma_{in}, \tag{29}$$

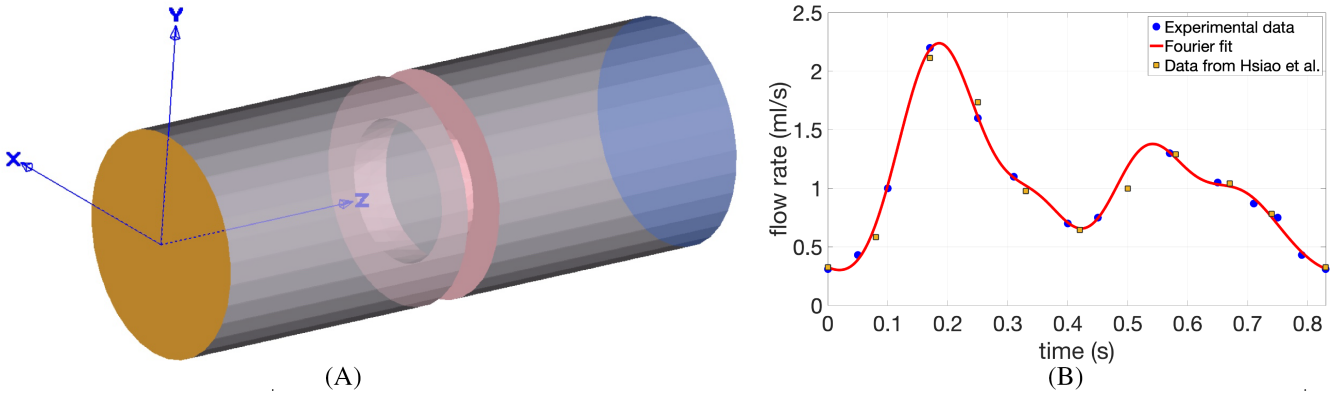

FIGURE 1 Definition of boundaries and inflow boundary conditions. (A) Color-coded boundaries: Γ_{in} in yellow, Γ_w in grey, Γ_{stent} in pink and Γ_{out} in blue. (B) Flow rate over one heartbeat imposed at inflow boundary Γ_{in}.

TABLE 1 Experimental data extrapolated from [3, 19].

time t [s]	**0**	**0.05**	**0.1**	**0.17**	**0.25**	**0.31**	**0.4**	**0.45**	**0.57**	**0.65**	**0.71**	**0.75**	**0.79**	**0.83**
$Q(t)$ [ml/s]	0.31	0.43	1.0	2.2	1.6	1.1	0.7	0.75	1.3	1.05	0.87	0.75	0.43	0.31

TABLE 2 Fourier coefficients of flow rate for each kth mode.

	0	**1**	**2**	**3**	**4**	**5**
a_k	2.146	−0.1646	−0.5616	−0.0658	−0.0129	0.0592
b_k	–	0.2692	0.1069	−0.1992	−0.1287	0.0633

where $C(A(t))$ is a function used to convert the flow rate $Q(t)$ from ml/s to mm/s depending on area $A(t)$ of the inlet surface Γ_{in} and $r_0 = 1.8$ mm is the radius of the artery. The function C is derived from the assumption that for parabolic profile, the peak velocity $v_{\max} = 2\bar{v} = 2\frac{Q}{A}$ where $\bar{v}$ is the average velocity and the flow rate Q and area A are evaluated at fixed time t. In general, the area $A(t)$ can change in time and the flow rate is given in $\frac{ml}{s}$, hence

$$C(A(t)) = \frac{2}{A(t)} C_{ml}^{mm^3}, \qquad \text{and} \qquad C_{ml}^{mm^3} = 1\frac{ml}{s} = 10^3 \frac{mm^3}{s}. \tag{30}$$

In the case of rigid wall, the circular inlet area $A(t) = A = \pi r_0^2$ is constant in time and the function $C(A)$ needs to be computed only once, independently of the flow rate of choice. Figure 1B shows the flow rate $Q(t)$ over one heart beat in the right coronary artery based on experimental values from [3, 19]. In particular, the blue dots are extrapolated with WebPlotDigitizer [35] from fig. 7b in [19], except for the minimum and maximum flow rate which are the only precise numerical values available. Hence, we specified a periodic minimum flow rate $Q(0s) = Q(0.83s) = 0.31\frac{ml}{s}$ and the maximum flow rate $Q(0.17s) = 2.2\frac{ml}{s}$, for a total of 14 evaluation points (see Table 1).

We interpolate the experimental data by means of Fourier series using MATLAB Curve Fitting Toolbox [20]. In the plot, the red line is obtained with five Fourier modes:

$$Q(t) = \frac{a_0}{2} + \sum_{k=1}^{5} \left[a_k \cos\left(k\frac{2\pi}{T}t\right) + b_k \sin\left(k\frac{2\pi}{T}t\right) \right], \tag{31}$$

where the coefficients a_i and b_i can be found in Table 2 and $T = 0.83$ s. For validation purposes, we extract the maximum velocity at various time snapshots from fig. 7a in [19] using WebPlotDigitizer [35]. After transforming the velocity back to flow rate, we compare these values to our interpolant in Figure 1B. A Fourier interpolation has multiple advantages: we can choose the period T to maintain the physiological periodicity of heart beats, we can tune the interpolation accuracy

choosing more Fourier modes and we impose a very smooth inflow velocity, which prevents possible instabilities due to the inflow boundary imposition. We use GLS-stabilized FEM with $\mathbb{P}_1 - \mathbb{P}_1$ element pair in space [8] and BDF2 multi-step method in time [4]. We linearize the convective term by means of Newton–Raphson method and solve the resulting linear system with a GMRES solver [38] and ILUT preconditioning [37].

The WSS is computed as:

$$\text{WSS} = |\boldsymbol{\tau}| = \mathbf{t} \cdot (\boldsymbol{\sigma}\mathbf{n}), \tag{32}$$

where $\mathbf{t}$ is the tangent vector, $\mathbf{n}$ is the outward normal vector and $\boldsymbol{\sigma}$ is the Cauchy stress tensor. The stress tensor for incompressible and viscous flows is defined as:

$$\boldsymbol{\sigma} = -p\mathbf{I} + 2\mu\mathbf{E}, \tag{33}$$

where $p = p(\mathbf{x}, t)$ is the pressure, μ is the dynamic viscosity, $\mathbf{E}(\mathbf{u}) = \frac{1}{2}\left(\nabla\mathbf{u} + \nabla\mathbf{u}^\top\right)$ is the rate of strain tensor and $\mathbf{u} = \mathbf{u}(\mathbf{x}, t)$ is the velocity vector. We compare two possible computations of WSS, that we refer to as $\boldsymbol{\tau}_1$ and $\boldsymbol{\tau}_2$ [22]. In the first case, we compute the WSS magnitude as the shear rate multiplied by the blood viscosity μ. The shear rate is given by:

$$\dot{\gamma} = \sqrt{-4II_{\mathbf{E}}} = \sqrt{2\mathbf{E} : \mathbf{E}} = \sqrt{2tr(\mathbf{E}^2)}, \tag{34}$$

where $II_{\mathbf{E}}$ is the second invariant of the tensor $\mathbf{E}$ and $tr(\mathbf{E}^2)$ is the trace and first invariant of the square tensor. This simplification is derived from the assumption that for parabolic unidirectional flows, the tangent vector $\mathbf{t} = \mathbf{t}_{\text{blood}}$ is uniquely defined, and $tr(E) = 0$. Thus, the WSS tensor $\boldsymbol{\tau}_1$ reduces to:

$$\text{WSS}_1 = |\boldsymbol{\tau}_1| = \mathbf{t} \cdot (\boldsymbol{\sigma}\mathbf{n}) = |2\mu\mathbf{E}\mathbf{n}| = \mu\dot{\gamma}, \tag{35}$$

where $\boldsymbol{\sigma}$ is defined in (33). If no assumptions on the flow are made, the WSS tensor $\boldsymbol{\tau}_2$ has the following expression:

$$\boldsymbol{\tau}_2 = \boldsymbol{\sigma}\mathbf{n} - [(\boldsymbol{\sigma}\mathbf{n}) \cdot \mathbf{n}]\mathbf{n} = 2\mu(\mathbf{E}\mathbf{n} - [(\mathbf{E}\mathbf{n}) \cdot \mathbf{n}]\mathbf{n}), \tag{36}$$

and its magnitude is defined as $\text{WSS}_2 = |\boldsymbol{\tau}_2|$.

3 | RESULTS

3.1 | Evolution of restenosis in a coronary arterial wall implanted with a XIENCE-V stent

The weak forms of the equations established in the preceding section in the Lagrangian coordinates are discretized spatially using trilinear hexahedral elements for the bulk of the arterial wall, and bilinear quadrilateral elements for the luminal surface. The temporal discretization is achieved using the backward-Euler method. This entire framework is then put into action using the finite element software package FEAP, utilizing user-defined elements. The necessary parameters are sourced from existing literature whenever possible. In cases where such data is unavailable, choices are made that lead to physiological macroscopic results.

In order to assess the viability of the modeling framework within a complex geometric context, a section of the human coronary artery containing an implanted XIENCE-V stent (manufactured by Abbott Vascular Inc.) is taken into consideration (see Figure 2). The region denoted as Γ_E^d signifies the area where the endothelium is assumed to have been completely removed due to the stent implantation procedure. Thus, the initial density ρ_E of endothelial cells (ECs) is set to zero within this region. Along the circular boundaries of the luminal surface (Γ_E^h), the EC density is initialized to match the healthy equilibrium value, initiating the process of endothelial recovery. Γ_{SS} designates the segment where the stent makes contact with the luminal side, and here the influx of drugs is predefined. The extremities in the longitudinal direction are restricted from experiencing longitudinal displacements, while the cylindrical surfaces on the non-luminal side are constrained against radial movements. The stent apposition area remains fixed against all forms of displacement.

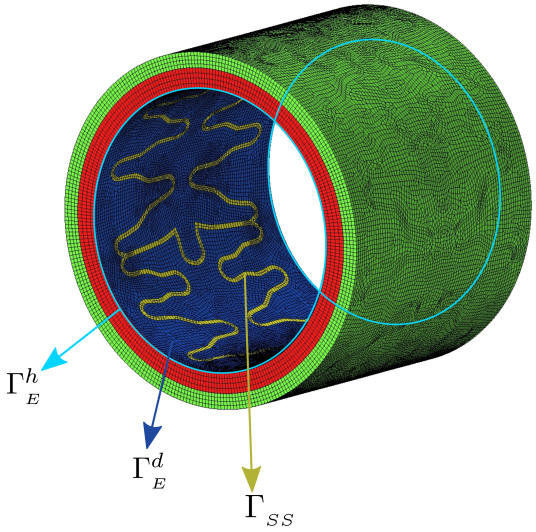

FIGURE 2 XIENCE-V stent in a coronary artery.

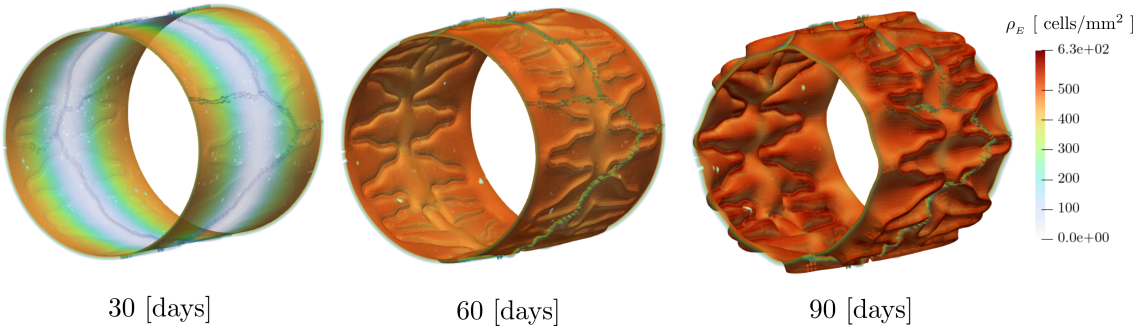

FIGURE 3 Endothelial recovery in the case of a bare metal stent implantation.

The established model is employed to simulate a period of 90 days. Figure 3 illustrates the process of endothelial recovery subsequent to the implantation of a bare-metal XIENCE-V stent. The initial phases of reendothelialization occur rather rapidly. However, the gradual and complete reestablishment of endothelial function takes a longer time, resulting in a substantial buildup of growth factors within the subintimal space. This, in turn, triggers an exacerbated growth response. The absence of the drug contributes to heightened restenotic growth as there are no anti-inflammatory effects within the arterial wall in this scenario although the endothelium recovers relatively quickly.

The impact of the drug level embedded in the stent struts, which is regulated by the parameter $\overline{q}_D^{ref}$ representing the peak drug influx, is evident in Figure 4. This parameter significantly influences the extent of restenotic growth, as the presence of rapamycin leads to a delay in the healing of the endothelium. The results point towards an optimality in the aforementioned parameter.

3.2 | Hemodynamic effects

In this section, we analyze the hemodynamics in stented arteries for a benchmark (ring stent) and a production case (ad-hoc XIENCE-V stent). We assume perfect contact between the stent and the artery and thus no indentation. All simulations are obtained with the highly parallelizable in-house code XNS [33] and were performed on the supercomputers JURECA at Forschungszentrum Juelich [25] and CLAIX 2018 at RWTH Aachen University. The ring stent simulation runs on 96 cores for 4.5 h to simulate three heart beats. The XIENCE-V stent simulations require approximately 7 h for one heart beat on 120 cores.

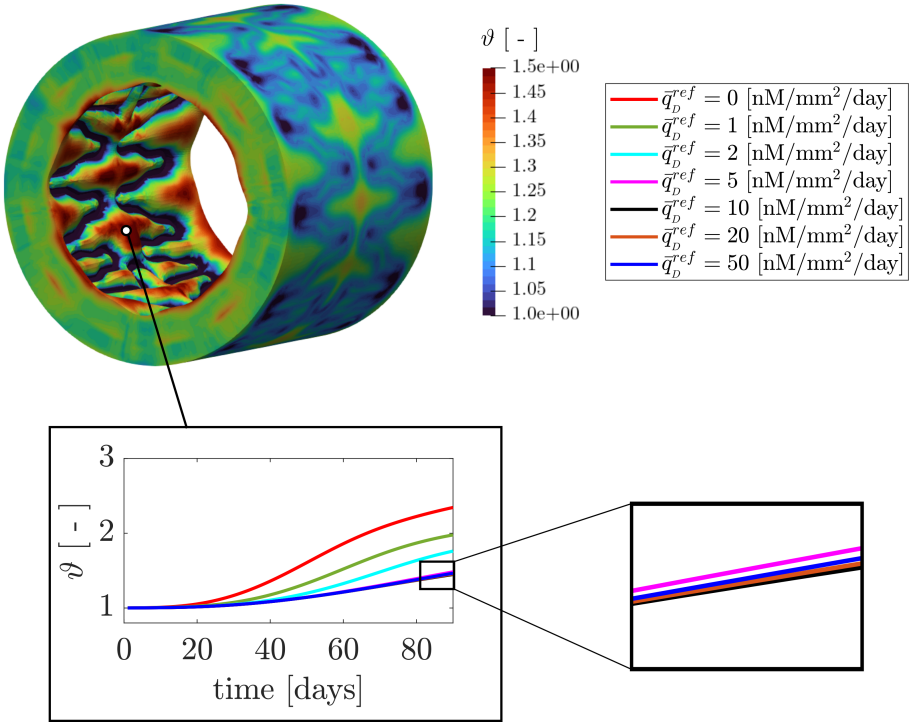

FIGURE 4 Evolution of growth stretch ϑ [-] for varying levels of drug embedment.

3.3 | Idealized artery with a ring stent

We first compare the hemodynamics of a benchmark configuration, that is, a ring stent with a square cross-section, to a healthy cylindrical artery segment. Both the stented and the healthy case have a radius of 1.8 mm and are 10 mm long. The ring stent thickness is 0.1 mm and we assume perfect contact between the stent and the artery.

Different indentation levels for this test case have been investigated in [32]. Figure 5B shows the velocity field at time $t = 0.25$ s in the artery segment with and without stent. If we compare velocity profiles at different time steps in Figure 5D,E, we observe that the flow is affected only in the stent proximity. In particular, bigger vortices appear downstream of the ring stent, see Figure 5A,C and their size is strictly dependent on the size of the strut. Figure 5F highlights the different vortex scales with a larger, rectangular stent. The ring stent can be regarded as a single strut in a complex stent design. Thus, we expect to observe similar hemodynamics close to all struts of the XIENCE-V stent.

An important parameter to analyze the well-being of the artery wall is the WSS: healthy values of WSS are between 0.8 and 1.5 Pa [23, 29]. Thus, we investigate the areas of low WSS where blood recirculation and induced inflammation is expected. The WSS measured on the healthy case in Figure 6B corresponds to the physiological baseline. Figure 6A,C displays WSS_1 on the artery wall and on the stent. In particular, we observe that the stent is subject to very high WSS while the wall immediately downstream of the stent has critically low WSS, in agreement with the results in [24]. By definition, WSS_1 and WSS_2 are equivalent in the healthy case but can show significant differences in the presence of a ring stent. In Figure 6D, we show the relative error

$$\epsilon_{\mathrm{WSS}} = \frac{|\mathrm{WSS}_1 - \mathrm{WSS}_2|}{\mathrm{WSS}_2}. \tag{37}$$

We pick four points on the artery wall to compare against the physiological values and to assess the influence of WSS_1 and WSS_2 over one heartbeat. Figure 7A,B shows that the stented artery has physiological values of WSS near inflow and outflow and that the computation of WSS_* is negligible far away from the stent. However, WSS values are critically low in the stent proximity and WSS_1 highly overestimates WSS values in the strut vicinity, see Figure 7C. The relative error in Figure 7D is between 40% and 70% over one heart beat and Figure 6D shows peaks of 200% in other nodes close to the

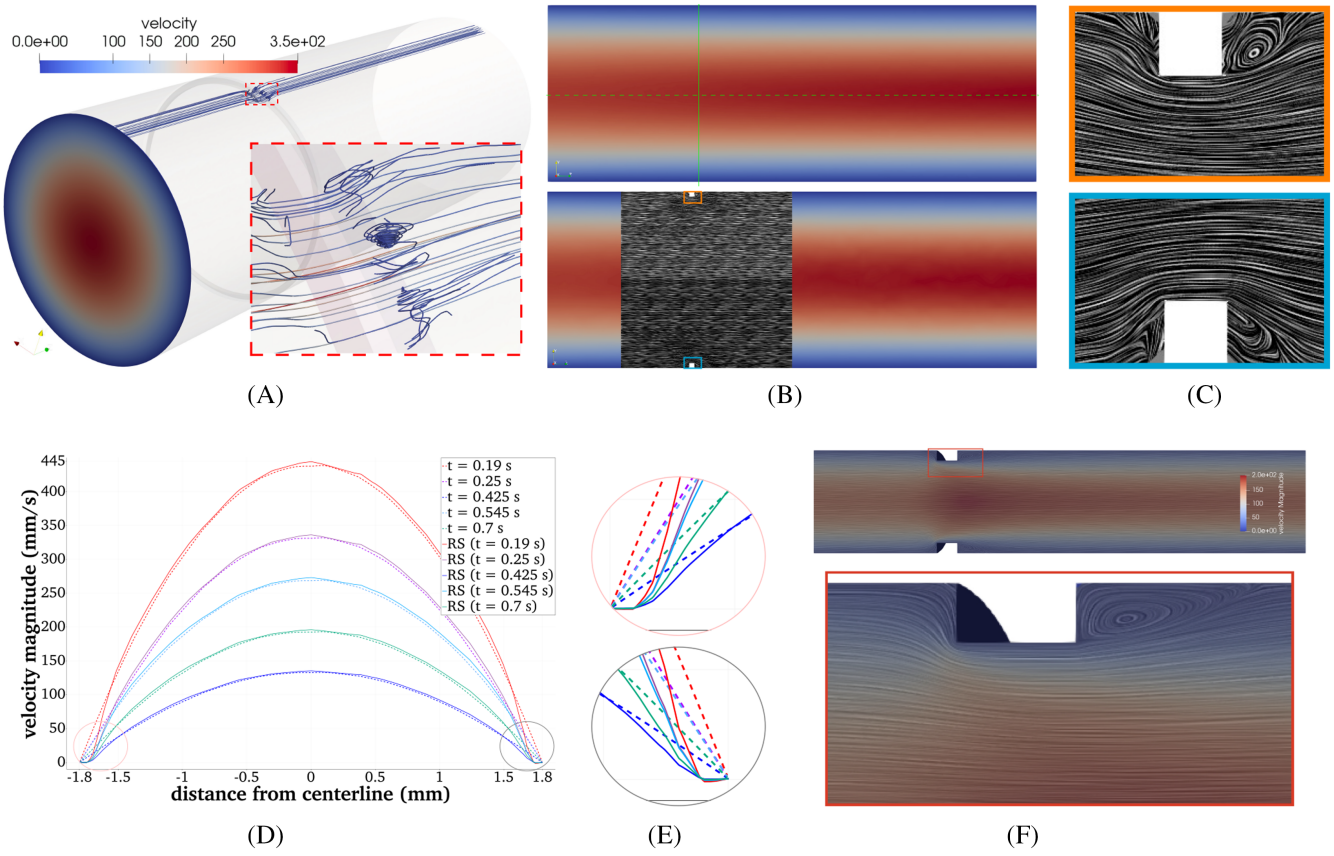

FIGURE 5 Velocity field comparison between stented and healthy artery: local vortices at $t = 0.25$ s with a ring stent in (A); velocity magnitude and streamlines at $t = 0.25$ s in (B), solid green line for flow profile comparison in (D) and centerline marked with a dashed green line; corresponding zoom on streamlines for ring stent in (C); comparison of flow profiles at different time snapshots, flow in the healthy case is marked with dashed lines and in the stented case (RS) with solid lines (D, E). Streamlines and local vortex comparison with rectangular ring stent in (F). (A) Ring stent vortices. (B) Velocity field. (C) Streamlines. (D) Flow profiles over solid green line, see (A, top). (E) Zoom. (F) Rectangular stent.

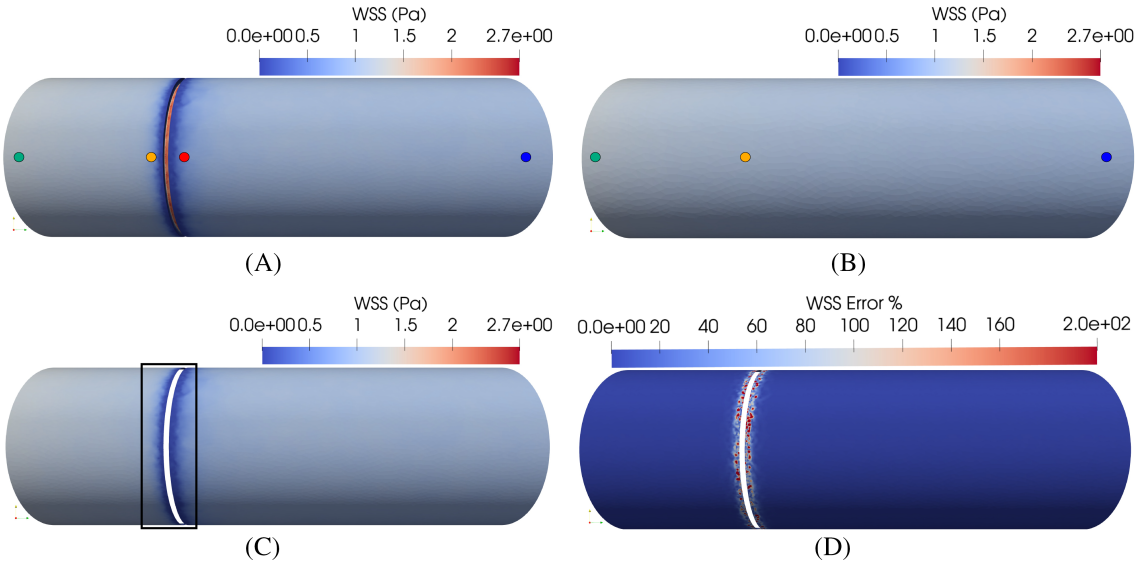

FIGURE 6 WSS and ϵ_{WSS} on stented and healthy artery. The colored dots in (A) and (B) correspond to the plot colors in Figure 7. From (C), zoom on rectangle can be found in Figure 11. (A) WSS on ring stent. (B) WSS on healthy artery. (C) WSS on stented wall. (D) ϵ_{WSS} on stented wall.

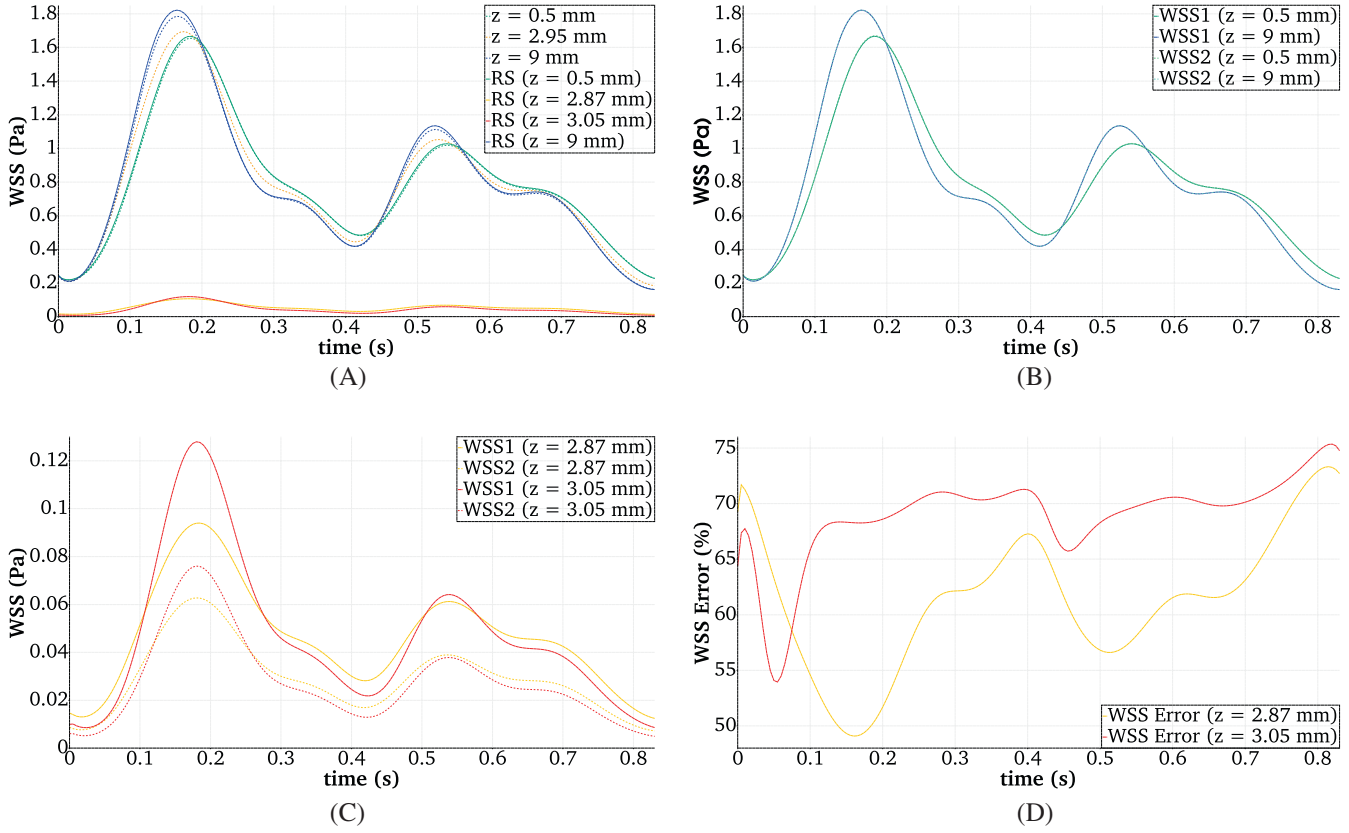

FIGURE 7 WSS and error comparison upstream, downstream and in the stent vicinity over one cycle T. Lines are color-coded according to the location in Figure 6. (A) WSS for healthy and ring stent (RS) case. (B) WSS_1, WSS_2 comparison for RS. (C) WSS_1, WSS_2 comparison for RS in stent vicinity. (D) ϵ_{WSS} for RS in the stent vicinity.

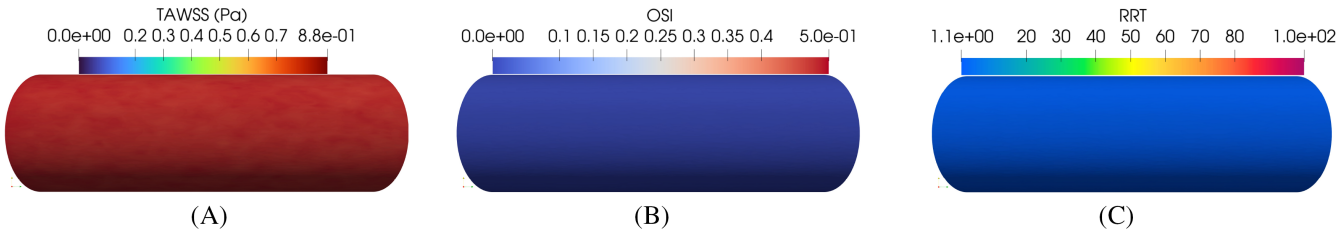

FIGURE 8 Physiological values on healthy artery. (A) TAWSS. (B) OSI. (C) RRT.

ring stent. The error distribution is scattered due to the fact that many nodes adjacent to the ring stent have zero values of WSS and therefore ϵ_{WSS} was set to zero.

We also tested the influence of the relative error on time-integrated quantities such as time-averaged WSS (TAWSS), oscillatory shear index (OSI), and relative residence time (RRT) given by the following expressions:

$$\text{TAWSS} = \frac{1}{T}\int_0^T |\boldsymbol{\tau}(t)|dt, \tag{38}$$

$$\text{OSI} = \frac{1}{2}\left(1 - \frac{|\int_0^T \boldsymbol{\tau}(t)dt|}{\int_0^T |\boldsymbol{\tau}(t)|dt}\right), \tag{39}$$

$$\text{RRT} = \frac{1}{(1-2\ \text{OSI})\text{TAWSS}}, \tag{40}$$

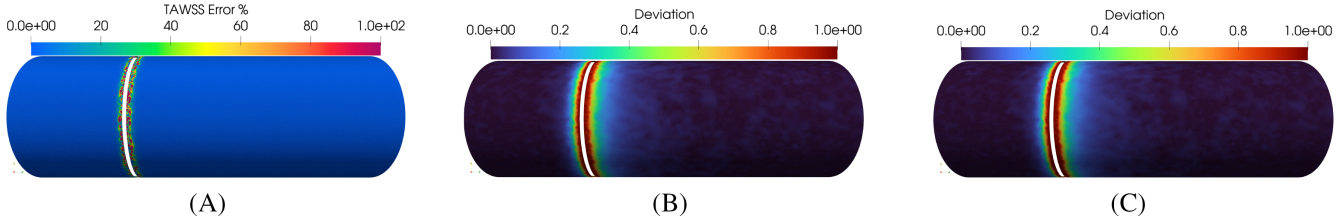

FIGURE 9 TAWSS error and deviation in artery with ring stent. (A) Error ϵ_{TAWSS}. (B) Deviation δ_1. (C) Deviation δ_2.

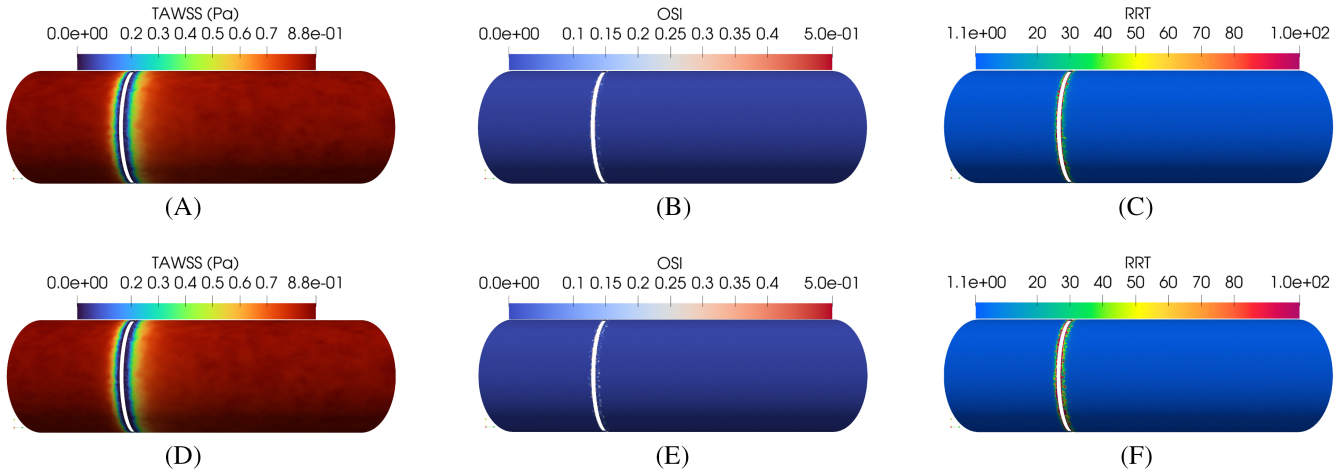

FIGURE 10 Artery wall with ring stent. (A) TAWSS_1. (B) OSI_1. (c) RRT_1. (D) TAWSS_2. (E) OSI_2. (F) RRT_2.

where $\boldsymbol{\tau} = \boldsymbol{\tau}_*$ and $*= 1, 2$. Figure 8 shows physiological values of approximately 0.8 Pa TAWSS, zero OSI, and RRT between 1.2 and 1.3 $\frac{1}{Pa}$.

These indicators are also compared on the artery wall for both WSS_* computations. It is worth pointing out that although the relative error can be locally very high, the normalized relative deviation

$$\delta_* = \frac{|\text{TAWSS}_* - \text{TAWSS}_{phys}|}{\text{TAWSS}_{phys}} \tag{41}$$

where $\text{TAWSS}_{phys} = 0.8$ Pa, is very similar for both computations of TAWSS (see Figure 9). This entails that the highest errors correspond to very low values of WSS (10^{-3} to 10^{-5}) and that WSS_1 overestimates shear stresses by one or two orders of magnitude.

Similarly to TAWSS, the overestimation error is further carried on to OSI_1 and RRT_1 as shown in Figure 10. In the former case, OSI is underestimated and some recirculation areas are neglected, while in the latter, RRT_2 shows more areas of high RRT, compared to RRT_1.

In Figure 11, we focus on the ring stent vicinity. We can qualitatively observe that TAWSS_1 overestimated the WSS values near the stent and the relative error up to 100% is carried after time integration from WSS_1 onto TAWSS, deviation δ, OSI and RRT.

This analysis concludes that even in the presence of very small struts (two orders of magnitude smaller than the artery length and one order smaller than the radius), the effect of recirculation and non-unidirectional flow cannot be neglected in the stent proximity. The results in the following section will only show values obtained from WSS_2, but for simplicity, we drop the subscript.

3.4 | Artery implanted with a XIENCE-V stent in *ad-hoc* configuration

For a more realistic application case, we simulate hemodynamics in an artery with XIENCE-V stent in expanded ad-hoc configuration and no indentation. The lumen with XIENCE-V stent has circa 2.5 M tetrahedron elements with an average

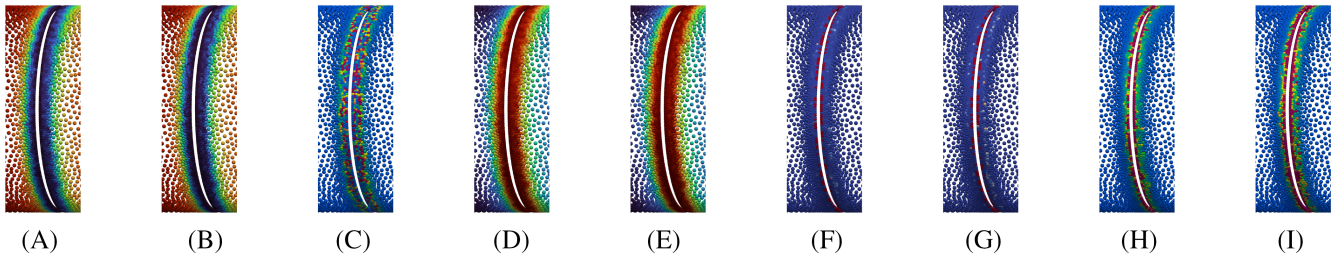

FIGURE 11 Zoom on artery wall in stent proximity, see Figure 6C. (A) $TAWSS_1$. (B) $TAWSS_2$. (C) ϵ_{TAWSS}. (D) δ_1. (E) δ_2. (f) OSI_1. (G) OSI_2. (H) RRT_1. (I) RRT_2.

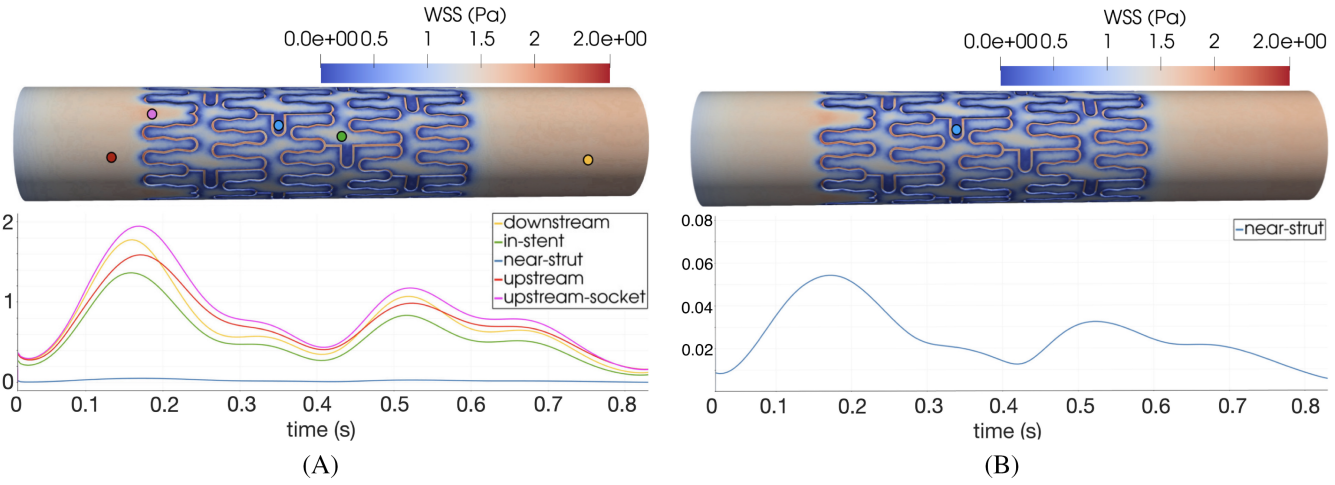

FIGURE 12 Side view of WSS in artery with XIENCE-V stent in ad-hoc configuration at $t = 0.25$ s (top) and over once cycle T (bottom). Lines are color-coded to the location on the artery wall. (A) Comparison of WSS on stented wall. (B) WSS in strut vicinity.

mesh size of 0.07 mm. To better analyze the different areas of WSS, we can look at a still-frame of the stented artery after 0.25 s in Figure 12A where we choose different points on the lumen-wall interface and analyze the WSS. The bottom plot depicts the WSS values of the highlighted areas over one cycle. Starting from the upstream wall, the red dot shows an overall physiological WSS over one cycle, and the pink dot highlights the socket area where the WSS is higher than any other region on the artery wall. The downstream wall (yellow) and the in-stent area (green) show physiological values, as well. Although the latter is lower than the average, it is still considered to be in an acceptable range. Extremely low values of WSS are detected near the struts, in particular within the U-shaped struts highlighted by the blue dot. The WSS values shown in Figure 12B are in the range of 10^{-2}, between 0.01 and 0.08 Pa, which is one order of magnitude lower than the healthy physiological range.

4 | CONCLUSIONS AND OUTLOOK

A high-fidelity multiphysics framework is herein presented that captures the intricate mechanism of ISR by modeling the significant mediators via suitable governing equations. The influence of the pharmacokinetics and pharmacodynamics in the vessel wall is investigated, which indicates the scope for optimization of drug embedment in modern DESs patient-specifically. In addition, the blood flow model is validated using an idealized healthy artery, approximated as a perfect cylinder, and the hemodynamics are compared to a ring stent test case. Particular emphasis is given to the influence of stent struts on micro dynamics: the analysis of streamlines in Section 3.3 shows that recirculation areas and vortices are located near the stent struts and that their geometry strongly influences them. Furthermore, two approaches for the computation of WSS and its derived indicators are compared, concluding that WSS_2 is a better measure. Critically low values of WSS are detected near the struts where inflammation and ISR occur, also in the application case with XIENCE-V

stent. Our analysis concludes that the mesh size of lumen computational domains in stented arteries has to be at least comparable to the stent thickness to ensure enough accuracy to capture local microdynamics. To reduce computational costs, targeted mesh refinement in the struts vicinity should be considered.

Future work shall then be focused on the coupling between the multiphysics arterial wall model and the hemodynamics model to exchange key indicators that throttle the restenotic response of arteries after stent implantation. Also, improvement in the computational efficiency of the high-fidelity models is to be achieved via the usage of reduced-integration finite elements and model-order reduction techniques.

ACKNOWLEDGEMENTS

The financial support of the Deutsche Forschungsgemeinschaft (DFG, German Research Foundation) for the projects "Drug-eluting coronary stents in stenosed arteries: medical investigation and computational modelling" (project number 395712048: RE 1057/44-1, RE 1057/44-2), "In-stent restenosis in coronary arteries–in silico investigations based on patient-specific data and meta modeling" (project number 465213526: RE 1057/53-1), a subproject of "SPP 2311: Robust coupling of continuum-biomechanical in silico models to establish active biological system models for later use in clinical applications—Co-design of modeling, numerics and usability", and "Modelling of Structure and Fluid-Structure Interaction during Tissue Maturation in Biohybrid Heart Valves", a subproject of "PAK961–Modeling of the structure and fluid–structure interaction of biohybrid heart valves on tissue maturation" (project number 403471716: RE 1057/45-1, RE 1057/45-2) is gratefully acknowledged. Additionally, this work was partially supported by the DFG via the project "GRK 2379: Hierarchical and Hybrid Approaches in Modern Inverse Problems" (project number 333849990).

The authors also gratefully acknowledge the computing time granted by the JARA Vergabegremium and provided on the JARA Partition part of the supercomputer CLAIX at RWTH Aachen University and on the supercomputer JURECA at Forschungszentrum Jülich. In addition, the authors gratefully acknowledge the computing time provided to them on the high-performance computer Lichtenberg at the NHR Centers NHR4CES at TU Darmstadt. This is funded by the Federal Ministry of Education and Research, and the state governments participating on the basis of the resolutions of the GWK for national high-performance computing at universities (https://www.nhr-verein.de/unsere-partner). Open Access funding enabled and organized by Projekt DEAL.

DATA AVAILABILITY STATEMENT

All FEAP-related FORTRAN subroutines and the Mathematica notebooks for algorithmic tangent computations via AceGen are made publicly available on Zenodo DOI: https://doi.org/10.5281/zenodo.10100652.

ORCID

Kiran Manjunatha https://orcid.org/0000-0003-1757-7909

REFERENCES

[1] M. Behbahani, M. Behr, M. Hormes, U. Steinseifer, D. Arora, O. Coronado, and M. Pasquali, A review of computational fluid dynamics analysis of blood pumps, Eur. J. Appl. Math. **20** (2009), no. 4, 363–397.

[2] M. Behr, D. Arora, O. Coronado, and M. Pasquali, Models and finite element techniques for blood flow simulation, Int. J. Comput. Fluid Dyn. **20** (2006), no. 3–4, 175–181.

[3] C. Bertolotti, V. Deplano, J. Fuseri, and P. Dupouy, Numerical and experimental models of post-operative realistic flows in stenosed coronary bypasses, J. Biomech. **34** (2001), no. 8, 1049–1064.

[4] K. E. Brenan, S. L. Campbell, and L. R. Petzold, *Numerical solution of initial-value problems in differential-algebraic equations*, Philadelphia, PA: SIAM, 1995.

[5] P. Budu-Grajdeanu et al., A mathematical model of venous neointimal hyperplasia formation, Theor. Biol. Med. Model. **5** (2008), 1–9.

[6] A. Caiazzo, D. Evans, J.-L. Falcone, J. Hegewald, E. Lorenz, B. Stahl, D. Wang, J. Bernsdorf, B. Chopard, J. P. Gunn, D. R. Hose, M. Krafczyk, P. V. Lawford, R. H. Smallwood, D. C. Walker, and A. G. Hoekstra, A complex automata approach for in-stent restenosis: Two-dimensional multiscale modelling and simulations, J. Comput. Sci. **2** (2011), 9–17.

[7] E. Cecchi, C. Giglioli, S. Valente, C. Lazzeri, G. F. Gensini, R. Abbate, and L. Mannini, Role of hemodynamic shear stress in cardiovascular disease, Atherosclerosis **214** (2011), no. 2, 249–256.

[8] J. Donea and A. Huerta, *Finite element methods for flow problems*, Hoboken, NJ: John Wiley & Sons, 2003.

[9] J. Escuer, M. A. Martinez, S. McGinty, and E. Pena, Mathematical modelling of the restenosis process after stent implantation, J. R. Soc. Interface **16** (2019), no. 157, 20190313.

[10] D. Evans, P. V. Lawford, J. P. Gunn, D. C. Walker, D. R. Hose, R. H. Smallwood, B. Chopard, M. Krafczyk, J. Bernsdorf, and A. G. Hoekstra, The application of multiscale modelling to the process of development and prevention of stenosis in a stented coronary artery, Philos. Trans. R. Soc. A Math. Phys. Eng. Sci. **366** (2008), 3343–3360.

[11] B. Fereidoonnezhad, R. Naghdabadi, S. Sohrabpour, and G. A. Holzapfel, J. Mech. Phys. Solids **101** (2017), 311–327.

[12] K. C. Garikipati, E. M. Arruda, K. Grosh, H. Narayanan, and S. Calve, A continuum treatment of growth in biological tissue: The coupling of mass transport and mechanics, J. Mech. Phys. Solids **52** (2004), 1595–1625.

[13] T. C. Gasser, R. W. Ogden, and G. A. Holzapfel, Hyperelastic modelling of arterial layers with distributed collagen fibre orientations, J. R. Soc. Interface **3** (2006), no. 6, 15–35.

[14] F. J. Gijsen, F. N. van de Vosse, and J. Janssen, The influence of the non-newtonian properties of blood on the flow in large arteries: Steady flow in a carotid bifurcation model, J. Biomech. **32** (1999), no. 6, 601–608.

[15] F. Guglietta, M. Behr, L. Biferale, G. Falcucci, and M. Sbrgaglia, On the effects of membrane viscosity on transient red blood cell dynamics, Soft Matter **16** (2020), no. 26, 6191–6205.

[16] S. Haßler, L. Pauli, and M. Behr, The variational multiscale formulation for the fully-implicit log-morphology equation as a tensor-based blood damage model, Int. J. Numer. Methods Biomed. Eng. **35** (2019), no. 12, e3262.

[17] R. He, L. Zhao, V. V. Silberschmidt, and Y. Liu, Mechanistic evaluation of longx02011;term inx02011;stent restenosis based on models of tissue damage and growth, Biomech. Model. Mechanobiol. **19** (2020), 1425–1446.

[18] H. Holthusen, C. Rothkranz, L. Lamm, T. Brepols, and S. Reese, Inelastic material formulations based on a co-rotated intermediate configuration—Application to bioengineered tissues, J. Mech. Phys. Solids **172** (2023), 105174. https://www.sciencedirect.com/science/article/pii/S0022509622003507.

[19] H.-M. Hsiao, K.-H. Lee, Y.-C. Liao, and Y.-C. Cheng, Hemodynamic simulation of intra-stent blood flow, Proc. Eng. **36** (2012), 128–136.

[20] The MathWorks, *Curve fitting toolbox*, United States, Natick, Massachusetts, 2021. https://mathworks.com/help/curvefit.

[21] C. Jenei, E. Balogh, G. T. Szabo, C. Dezsi, and Z. Koszegi, Cardiol. J. **23** (2016), no. 4, 365–373.

[22] L. John, P. Pustějovská, and O. Steinbach, On the influence of the wall shear stress vector form on hemodynamic indicators, Comput. Vis. Sci. **18** (2017), 113–122.

[23] D. H. Kim, S.-J. Heo, S.-H. Kim, J. W. Shin, S. H. Park, and J.-W. Shin, Shear stress magnitude is critical in regulating the differentiation of mesenchymal stem cells even with endothelial growth medium, Biotechnol. Lett. **33** (2011), 2351–2359.

[24] K. C. Koskinas, Y. S. Chatzizisis, A. P. Antoniadis, and G. D. Giannoglou, Role of endothelial shear stress in stent restenosis and thrombosis: Pathophysiologic mechanisms and implications for clinical translation, J. Am. Coll. Cardiol. **59** (2012), no. 15, 1337–1349.

[25] D. Krause and P. Thörnig, Jureca: modular supercomputer at Jülich supercomputing centre, J. Large-Scale Res. Facilit. **4** (2018), A132.

[26] A. Leuprecht and K. Perktold, Computer simulation of non-Newtonian effects on blood flow in large arteries, Comput. Methods Biomech. Biomed. Engin. **4** (2001), no. 2, 149–163.

[27] V. A. Lubarda and A. Hoger, On the mechanics of solids with a growing mass, Int. J. Solids Struct. **39** (2002), 4627–4664.

[28] K. Manjunatha, N. Schaaps, M. Behr, F. Vogt, and S. Reese, Computational modeling of in-stent restenosis: Pharmacokinetic and pharmacodynamic evaluation, Comput. Biol. Med. **167** (2023), 107686. https://www.sciencedirect.com/science/article/pii/S0010482523011514.

[29] T. M. Maul, D. W. Chew, A. Nieponice, and D. A. Vorp, Mechanical stimuli differentially control stem cell behavior: Morphology, proliferation, and differentiation, Biomech. Model. Mechanobiol. **10** (2011), 939–953.

[30] A. McQueen, J. Escuer, A. F. Schmidt, A. Aggarwal, S. Kennedy, C. McCormick, K. Oldroyd, and S. McGinty, An intricate interplay between stent drug dose and release rate dictates arterial restenosis, J. Control. Release **349** (2022), 992–1008. https://www.sciencedirect.com/science/article/pii/S0168365922004722.

[31] G. Nakazawa, A. V. Finn, M. Joner, E. Ladich, R. Kutys, E. K. Mont, H. K. Gold, A. P. Burke, F. D. Kolodgie, and R. Virmani, Delayed arterial healing and increased late stent thrombosis at culprit sites after drug-eluting stent placement for acute myocardial infarction patients: An autopsy study, Circulation **118** (2008), no. 11, 1138–1145.

[32] S. Nerzak and H. Volgmann, *Wall shear stress and blood residence time as risk factors in stented arteries, RWTH-2023-00950*, Aachen, Germany: RWTH Aachen University, 2021. https://publications.rwth-aachen.de/record/889072.

[33] L. Pauli and M. Behr, On stabilized space-time FEM for anisotropic meshes: Incompressible Navier-stokes equations and applications to blood flow in medical devices, Int. J. Numer. Methods Fluids **85** (2017), no. 3, 189–209.

[34] E. K. Rodriguez, A. Hoger, and A. D. McCulloch, Stress-dependent finite growth in soft elastic tissues, J. Biomech. **27** (1994), no. 4, 455–467.

[35] A. Rohatgi. Webplotdigitizer: Version 4.6, 2022. https://automeris.io/WebPlotDigitizer.

[36] F. Rossi, T. Casalini, E. Raffa, M. Masi, and G. Perale, Bioresorbable polymer coated drug eluting stent: A model study, Mol. Pharm. **9** (2012), no. 7, 1898–1910.

[37] Y. Saad, *Iterative methods for sparse linear systems*, Philadelphia, PA: SIAM, 2003.

[38] Y. Saad and M. H. Schultz, Gmres: A generalized minimal residual algorithm for solving nonsymmetric linear systems, SIAM J. Sci. Stat. Comput. **7** (1986), no. 3, 856–869.

[39] J. Sasse, *Shear thinning constitutive model in stented arteries*, Master's thesis, Aachen, Germany: RWTH Aachen University, 2020. https://publications.rwth-aachen.de/record/889071.

[40] H. Tahir, A. G. Hoekstra, E. Lorenz, P. V. Lawford, D. R. Hose, J. Gunn, and D. J. W. Evans, Multi-scale simulations of the dynamics of in-stent restenosis: Impact of stent deployment and design, Interface Focus **1** (2011), no. 3, 365–373.

[41] H. Zahedmanesh, H. V. Oosterwyck, and C. Lally, A multi-scale mechanobiological model of in-stent restenosis: Deciphering the role of matrix metalloproteinase and extracellular matrix changes, Comput. Methods Biomech. Biomed. Engin. **17** (2014), 813–828.

[42] P. S. Zun, A. I. Svitenkov, and A. G. Hoekstra, Effects of local coronary blood flow dynamics on the predictions of a model of in-stent restenosis, J. Biomech. **120** (2021), 110361.

How to cite this article: K. Manjunatha, A. Ranno, J. Shi, N. Schaaps, P. Nilcham, A. Cornelissen, F. Vogt, M. Behr, and S. Reese, *A continuum chemo-mechano-biological model for in-stent restenosis with consideration of hemodynamic effects*, GAMM-Mitteilungen. **48** (2025), e202370008. https://doi.org/10.1002/gamm.202370008